Role of atomic variability in dielectric charging: A first-principles-based multiscale modeling study

R. P. Vedula,[1] S. Palit,[1] M. A. Alam,[1,*] and A. Strachan[2,†]

[1]*School of Electrical and Computer Engineering, Purdue University, West Lafayette, Indiana 47907, USA*

[2]*School of Material Science and Engineering and Birck Nanotechnology Center, Purdue University, West Lafayette, Indiana 47907, USA*

(Received 19 December 2012; revised manuscript received 28 February 2013; published 13 November 2013)

We present a dielectric charging model that combines *ab initio* calculations of trap levels with a continuum-level transport model and apply it to interpret charging currents in amorphous silicon nitride. Density functional theory calculations on an ensemble of structures predict a distribution of electron trap levels up to 1.8 eV below the conduction band edge and provide insight into the physical trapping mechanisms. Incorporating this information in the continuum model, as opposed to the standard approach of a single adjustable trap level, not only leads to a more accurate description of experimental current transients in metal-insulator-metal capacitors, but also to a more precise and physical determination of associated material properties such as metal-dielectric barrier height.

DOI: 10.1103/PhysRevB.88.205204 PACS number(s): 71.15.Mb, 61.72.J−, 71.55.−i, 73.23.−b

I. INTRODUCTION

Amorphous dielectrics are ubiquitous in electronics, energy conversion, displays, and many other applications. The presence of point defects in these materials leads to dielectric charging (the semi-permanent trapping of charges), which in turn governs either the operation (as in nonvolatile memories) or time-dependent performance degradation (as in gate dielectrics) of these devices. Amorphous silicon nitride (a-Si_3N_4) is one such widely used dielectric in applications such as Radio-Frequency Micro-Electro-Mechanical Systems (RF-MEMS),[1] nonvolatile memories,[2] surface passivants in crystalline solar cells,[3] and as ionic diffusion barriers in a-Si thin film solar cell fabrication.[4] Unfortunately, traditional fabrication using chemical/physical vapor deposition methods[5] create an inherently large concentration of point defects in these dielectrics.[6] While these trap centers are central to the operation of nonvolatile memories, they create undesirable shifts in actuation voltages leading to catastrophic stiction in RF-MEMS[7] and efficiency degradation in solar cells.[8] Accurate models to predict dielectric charging are, therefore, key to understanding the performance and reliability of a wide variety of devices. Furthermore, a connection to the underlying atomic-level processes can provide insights which would allow engineering of these materials for improved performance.

A fundamental challenge to predictive modeling of charging in amorphous dielectrics over a wide range of timescales, voltages, and temperatures is the intrinsic atomic variability in their structures, which leads to a distribution of associated properties (e.g., defect formation energies and electronic energy levels). Most characterization methodologies yield integrated signals (both spatially and energetically) that cannot be uniquely mapped back to the intrinsic defect distribution.[9,10] Instead, an effective defect level is assigned to interpret the characterization data. However, it is well known that simplistic models based on single-level trapping often have limited range of validity and can lead to unphysical parameterization.[11] Therefore, the need for predictive multiscale modeling has long been recognized.[12] The lack of a long-range atomic order in the amorphous structures further complicates the generation of representative materials required for capturing the atomic-level processes responsible for charging, including the role of inherent variability.[13,14]

In this paper, we demonstrate that a multiscale model that couples first-principles calculations of the distribution of trap levels with a continuum dielectric charging model allows for an unambiguous, physics-based prediction of trapping kinetics in amorphous materials. Using current transient measurements on metal-insulator-metal (MIM) capacitors fabricated for this purpose, we show that by replacing a single adjustable trap depth (the most sensitive parameter in the prediction of current transients) in the continuum simulation with a distribution of trap levels from *ab initio* calculations leads not only to a reduction in the empiricism of current state-of-the-art models, but also enables a more accurate description of experimental current transients, and more notably, a precise determination of additional calibrated material parameters. The approach is broadly applicable and is expected to describe physical phenomena across various length and time scales necessary to accurately predict the lifetime of devices being operated at different temperatures and voltage biasing conditions.

II. MULTISCALE DIELECTRIC CHARGING MODEL

We now describe the multiscale model by first considering the characterization of electron trap energy levels of intrinsic defects in a-Si_3N_4 followed by a description of the continuum dielectric charging model.

A. First-principles characterization of electron trap levels and their physical mechanisms

Energy levels are obtained from charge-state density functional theory (DFT) calculations over the intrinsic point defects in an ensemble of representative a-Si_3N_4 structures. An ensemble of a 112-atom, periodic, structures are generated by molecular dynamics annealing simulations starting from independent liquid samples, followed by DFT stress relaxations (both lattice parameters and atom positions were relaxed for generation of these structures).[13,14] This approach not only predicts the intrinsic point defects, but also defect-free structures that can be used as a reference for establishing the band-edges.[13,14] Point defects are defined as atoms that deviate from their ideal coordination (alternating four coordinated Si and three coordinated N atoms). A detailed description of structure generation and defect characterization can be found

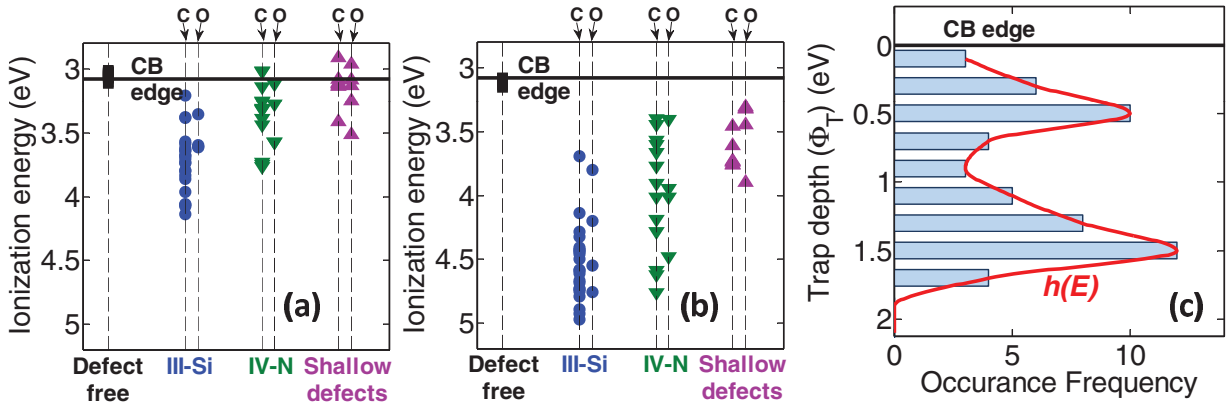

FIG. 1. (Color online) (a) Instantaneous and (b) thermodynamic electron trap-energy levels of the ensemble of a-Si_3N_4 structures categorized according to the defect relaxation mechanisms. ("C" indicates the most common relaxation mechanism, and "O" indicates the other observed relaxation mechanisms.) (c) Histogram representing the distribution of thermodynamic defect levels.

in Ref. 14. Charge-state relaxation calculations (atomic positions only) are performed for each point defect in the ensemble of structures by placing an electron in the defect site (defect-free structures are charged by locating the charge at random). The local moment counter-charge (LMCC) method[15,16] is used to address the potential divergence that originates in a periodic simulation with nonzero net charge. Energy levels are then obtained from total energy differences between DFT calculations of charged and neutral states using an electronic chemical potential from neutral defective supercell, as implemented in the finite defect supercell model.[16] The energy contribution from bulk polarization is accounted by using a classical model proposed by Jost.[17] The accuracy of this approach, using semilocal exchange-correlation functionals, has been previously demonstrated for Si,[16] GaAs,[18] and amorphous silica.[19]

All calculations in this work are performed within the Perdew-Burke-and-Ernzerhof (PBE) approach to the generalized gradient approximation[20] using localized Gaussian basis set in linear combination of atomic orbitals approach implemented in SeqQuest[21] code from Sandia National Laboratories. Troullier-Martins pseudopotential for N atoms[22] and Hamann pseudopotentials for Si[23] were used to describe core-valence electron interactions. A convergence criteria of 1.36×10^{-4} eV and 1×10^{-3} Ry/Bohr were used for self-consistent field convergence and force relaxation, respectively. A Γ-point sampling was used to perform Brillouin-zone integrations.

The charge state relaxation calculations were performed on a total of 86 structures: 55 defective and 31 defect-free structures. While a substantial number of these structures were defect-free, the defective structures contained between 2–6 defects per supercell. We observed that the electrons were always captured by the energetically most favorable defect in the supercell, irrespective of the defect where charge was initially placed. Thus, for a given structure, we observed only one possible relaxation mechanism, irrespective of where the electron was initially placed.

Instantaneous transition energy levels, obtained from charge state calculations using the neutral atomic configuration, are shown in Fig. 1(a) along with the thermodynamic energy levels obtained after the structures are relaxed under the presence of the charge [Fig. 1(b)]. Figures 1(a) and 1(b) provide individual energy levels categorized by an atomistic trapping mechanism, and Fig. 1(c) shows the distribution of thermodynamic energy levels for electron capture obtained over the entire set of defects in the ensemble of structures. In most cases, significant structural relaxation is observed when a charge is trapped by a defect. This effect is due to the localization of charge at a defect site and is clearly observed in Figs. 1(a) and 1(b), where a significant energy difference between instantaneous and thermodynamic levels is seen. Interestingly, the defect-free cells exhibit little atomic relaxation when charged, and the energy difference between thermodynamic and instantaneous transition energies is very small; this indicates that the charge is delocalized in the conduction band (CB). We therefore use the average energy values of defect-free structures to define the CB edge. From these calculations, we establish the CB edge to be at 3.11 eV.

On establishing the reference for the CB edge, we find that the thermodynamic $(-1/0)$ transition states span a continuous range of energy levels from 0.2–1.8 eV below the CB edge [Fig. 1(c)]. These results are in excellent agreement with recent trap spectroscopy by charge injection and sensing (TSCIS) experiments[24] that report a range of energy levels between 0.8–1.8 eV below the CB edge (energies below 0.8 eV could not be probed by the experimental setup). The predicted distribution exhibits two distinct peaks with the thermodynamically more favorable traps centered around 1.5 eV below the CB; this is in excellent correlation with defect energy levels corresponding to maximum trap density observed in TSCIS experiments. In addition to the distribution of energy levels, the *ab initio* charge state calculations provide detailed information about defect-specific distribution of energy levels and their corresponding trapping mechanisms. Two defects dominate electron trapping in a-Si_3N_4: undercoordinated Si atoms (III-Si known as K centers) and overcoordinated IV-N atoms. From Fig. 1(b), we find that undercoordinated III-Si atoms provide the deepest traps; however, their distribution overlaps with that of overcoordinated IV-N atoms. This result highlights the importance of the

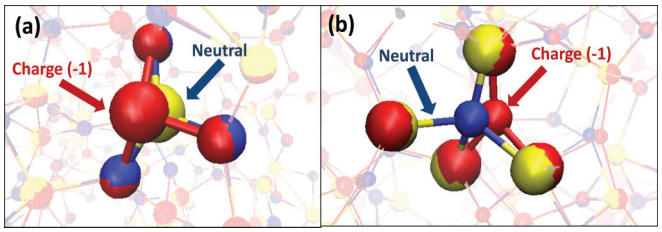

FIG. 2. (Color online) Atomic snapshots of the dominant electron-trapping mechanisms (a) undercoordinated III-Si defect on capturing an electron changes its hybridization from sp^2-planar configuration (average bond angle: 119.84°) to sp^3-tetrahedral hybridization (average bond angle: 119.84°). (b) IV-N defect breaks a bond and changes hybridization from sp^3-tetrahedral configuration to sp^2-planar configuration on electron trapping.

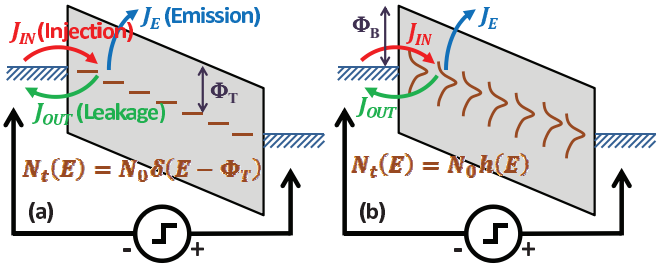

FIG. 3. (Color online) The band diagram of an amorphous dielectric in a MIM capacitor system under an applied bias for (a) single-level traps and (b) multiple-level traps. The trapping/detrapping current fluxes J_{in}, J_{out}, and J_e and the physical interpretations of trap depth (Φ_T) and barrier height (Φ_B) are indicated. The trap distribution function $h(E)$ in (b) is obtained from the distribution in Fig. 1(c).

intrinsic atomic variability in amorphous dielectrics and that single levels are unable to capture the physics of even a single topological defect type.[25,26]

The most commonly observed electron-trapping mechanism for III-Si atoms, leading to energy levels marked as "C" in Fig. 1(b), involves a transition between a near planar sp^2 hybridization (with average bond angle of 119.84°) to an sp^3 hybridized tetrahedral configuration (with average bond angle around Si of 109.4°). Snapshots from our simulations corresponding to this mechanism are shown in Fig. 2(a). In addition, two other trapping mechanisms [energies noted as "O" in Fig. 1(b)] for III-Si are observed, and their description is provided in Appendix A. While the III-Si defect is widely recognized as the most probable electron trap in a-Si_3N_4,[26–28] our DFT calculations show that IV-N defects also contribute states near the midgap. The most common trapping mechanism for IV-N defects involves the over-coordinated N atom starting in a tetrahedral (sp^3) configuration in the neutral cell with average bond angle of 109.45° [see Fig. 2(b)]. Electron trapping leads to the breaking of a Si-N bond, causing a change in the hybridization of the N atom to an sp^2 (ideally coordinated) structure. An accompanying decrease in average bond length by 0.15 Å and increase in average bond angle to 119.82° is observed. The bond breaking process upon electron trapping leads to a tetrahedral III-Si defect in the structure. Approximately 77% of the structures exhibiting these relaxations lacked III-Si defects initially. Importantly, however, the remaining 24% of the structures also contained a planar III-Si defect, but trapping by the IV-N atom was more favorable. This indicates that once intrinsic fluctuations are accounted for, the IV-N defect can be a thermodynamically favorable electron trap. These rigorous calculations provide detailed information regarding atomistic relaxations induced by charge trapping contribute information that is inaccessible through band-structure calculations. Our observations on IV-N defect contradict prior conclusions based on Kohn-Sham density of states[14] and GW[29] calculations, which indicated that over-coordinated defects do not lead to states in the band gap and consequently cannot trap charges. Similar to III-Si, depending on the defect's local atomic structure, these defects also contribute to a distribution of gap states. Other less likely trapping mechanisms, resulting in shallow defect states, are discussed in Appendix A.

B. Meso-scale continuum dielectric charging model

Once the distribution of defect levels is available, a meso-scale continuum model describing charge trapping dynamics is used to calculate transient leakage currents.[11] The model is based on current continuity from three trapping/detrapping fluxes: J_{in} (electron injection from the metal into the trap levels), J_{out} (electron leakage from trap levels into the metal), and J_e (electron emission from the traps into the dielectric CB; see Fig. 3). J_{in} and J_{out} are trap-assisted tunneling fluxes, calculated using a modified form of the Tsu-Esaki equation.[30] The tunneling/transmission coefficient is computed using the Wentzel-Kramers-Brillouin (WKB)[31] approximation. J_e is assumed to be a electric-field assisted, temperature-activated Frenkel-Poole (FP) emission process.[32] The following equations[11] are used to describe these current fluxes:

$$\frac{dJ_{\text{in}}(x)}{dx} = \int \Gamma_{\text{in}}(x,E)[N_t(x,T,E) - n_t(x,E)]dE, \quad (1)$$

$$\frac{dJ_{\text{out}}(x)}{dx} = \int \Gamma_{\text{out}}(x,E)[n_t(x,E)]dE, \quad (2)$$

$$\frac{dJ_e(x)}{dx} = \int \Gamma_e(x,E)[n_t(x,E)]dE. \quad (3)$$

Here x is the distance of a trap location in the dielectric from the contact; dx is a differential element in space (grid size); E is the energy measured from the CB edge; $N_t(x,T,E)$ is the energy-resolved density of trap states inside the dielectric and $n_t(x,E)$ is the corresponding density of occupied traps; $\Gamma_{\text{in}}(x)$, $\Gamma_{\text{out}}(x)$, and $\Gamma_e(x)$ (see Appendix B) are the injection, leakage, and emission flux coefficients that depend on the model parameters: barrier height (Φ_B), capture cross section of the trap (σ), electron effective mass in the dielectric (m^*), the FP emission attempt frequency (γ), and the dielectric constant of the dielectric (ϵ). The temperature dependence on the density of trap states is assumed to be Arrhenius with activation energy of E_a, i.e., $N_t(x,T,E) = N_t^0(x,E)\exp(-\frac{qE_a}{k_BT})$. It is observed that for most metal-dielectric interfaces, the barrier for electron injection into the dielectric (difference in energy between the dielectric CB and metal work function) is greater than the barrier for hole injection (difference in energy between the dielectric valence band and metal work function). For values of common contact metal work functions, and the band-gap information for common dielectrics, the reader is referred

to Refs. 33 and 34. As a result, dielectric charging due to holes is significantly smaller than that of electrons and is not considered in this model.

The continuity equation for the total trap occupancy at position x is given by

$$q\frac{d}{dt}\int n_t(x,E)dE = \frac{dJ_{\text{in}}(x)}{dx} - \frac{dJ_{\text{out}}(x)}{dx} - \frac{dJ_e(x)}{dx}. \quad (4)$$

Equation (4) is solved analytically in conjunction with Eqs. (1)–(3) in terms of the flux coefficients Γ_{in}, Γ_{out}, and Γ_e for obtaining the transient solution of $n_t(x,E)$. The transient current at the contact is given by

$$\begin{aligned} J_{\text{contact}}(t) &\equiv \int (dJ_{\text{in}} - dJ_{\text{out}}) \\ &= \int\int [\Gamma_{\text{in}} N_t - (\Gamma_{\text{in}} + \Gamma_{\text{out}}) n_t] dE dx \\ &= \int\int \left[C_1(x,E) + C_2(x,E) \exp\left(-\frac{tC_0(x,E)}{q}\right)\right] \\ &\quad \times dE dx, \end{aligned} \quad (5)$$

where the values C_0, C_1, and C_2 are given by $\Gamma_{\text{in}} + \Gamma_{\text{out}} + \Gamma_e$, $(\Gamma_{\text{in}}\Gamma_{\text{out}} N_t)/C_0$, and $\Gamma_{\text{in}}(\Gamma_{\text{out}} + \Gamma_e) N_t/C_0$, respectively.

III. LEAKAGE TRANSIENT EXPERIMENTS AND MODEL CALIBRATION RESULTS

The multiscale model described above is now used to model leakage current transients measured on MIM capacitors. These capacitors have a cross-sectional area of 2 mm $\times$2 mm. A 200-nm-thick dielectric was deposited with a plasma-enhanced CVD (Chemical Vapor Deposition) process using Axic Benchmark 800 PECVD system at 300 °C and 400 mTorr with 120 sccm 5% SiH_4 and 100 sccm NH_3. The leakage transients were measured across a temperature range of 300 K–360 K and voltage bias range of 10 V–20 V using Keithley 4200SCS Source-Measure Unit. Current leakage transients are measured between 1–100 s of application of a step bias, and the experimental results are shown as dots in Figs. 4(a)–4(c).

This experimental data was used to calibrate the undetermined physical parameters associated with the dielectric charging model using a simulated annealing optimization framework (see Appendix C for details regarding cost function and ranges for exploring the parameter space). Two hundred independent simulated annealing runs were performed to estimate the uncertainty in the resulting parameters. From Figs. 4(a)–4(c) we observe that the dielectric charging model, based on trap level distribution obtained from the first-principles calculations, captures the essential trends of the experimental data over a range of voltages, temperatures, and times. In order to assess the importance of the theoretically predicted distribution of trap levels, we also fit the experimental data with the same continuum model and optimization procedure but using the traditional approach of a single trap energy level being taken as a free, adjustable parameter (see Fig. 3). Table I shows the comparison of the minimum of the optimized errors from the 200 independent optimization runs and the corresponding optimized parameters obtained by simulated annealing using *ab initio*-informed trap levels and with trap levels used as fitting parameters. For a reference, the complete distributions of optimized errors and model parameters obtained from the 200 independent optimization runs can be found in the Supplemental Material.[35] A sensitivity analysis (see Appendix D) shows that the trap depth and barrier height are the most sensitive parameters to the dielectric charging model across all time scales, applied voltages, and temperature conditions. This highlights the significant reduction in empiricism in the multiscale model by determining the most sensitive parameter from *ab initio* predictions.

Though the overall descriptions of transient currents of both models are comparable, the *ab initio*-informed model leads to a reduction in the relative error of approximately 34% while eliminating the most sensitive parameter (trap depth) as a tunable parameter (see Fig. 6 in Appendix D). More importantly, without *ab-initio* input, the calibrated parameters show an unphysical variability; for example, the barrier height for electrons to tunnel into the dielectric (the second-most sensitive parameter in the model) is predicted to vary between ~1.2 to 2.2 eV using the tunable trap energy level, while the *ab initio*-informed model determines this physical parameter with high accuracy [see Fig. 4(d)]. Obtaining a precise value of the metal-dielectric barrier height is critically important for reliability quantification; using the results of the single trap level model exhibits the risks associated with

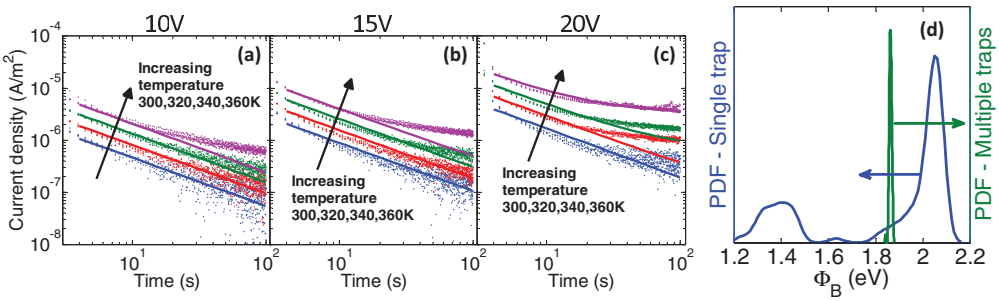

FIG. 4. (Color online) (a–c) Experimental current transients (dots) measured on MIM capacitors over a range of voltages (10–20 V) and temperatures (300–360 K). Lines represent fits to the data using first-principles informed dielectric charging model. (d) Comparison of the PDFs of the optimized values of the barrier height (Φ_B) values resulting from 200 statistically independent simulation-annealing optimizations for dielectric charging model with trap depth as fitting parameter (blue) and dielectric charging model using trap distribution obtained from first-principles calculation (green).

TABLE I. List of model parameters, symbols, and units (first column) and the parameter set corresponding to the minimum error value obtained for fitting the dielectric charging model with experimental data using trap depth as adjustable parameter (second column) and first-principles informed trap-depth information (third column).

Variable	Single trap level as an adjustable parameter	First-principles informed trap levels
Barrier height Φ_B (eV)	1.46	1.86
Trap density N_T (m^{-3})	8.93×10^{23}	1.11×10^{24}
Effective mass m^*	0.600	0.131
Capture cross section σ (m^2)	1.00×10^{-22}	1.00×10^{-19}
Escape attempt frequency γ (s^{-1})	8.79×10^{13}	1.98×10^{11}
Dielectric constant ϵ	3.04	3.00
Activation energy E_a (eV)	0.219	0.225
Trap depth Φ_T (eV)	1.59	from first-principles calculations
Error	0.299	0.201

over-parameterized models. In addition, we observe that the ranges for capture cross-section (σ) and effective mass (m^*) are more physical and consistent with prior literature for the multiple trap model.

IV. CONCLUSIONS

To summarize, we have introduced a multiscale model for dielectric charging in amorphous dielectrics where key information (defect energy-level distributions, charge states, and energy relaxations) are obtained from rigorous first-principles calculations that capture the intrinsic variability in the amorphous network. This information not only reduces the empiricism (number of adjustable parameters) in the model but also leads to a predictive model that is more accurate over broad range of voltages, temperatures, and time scales and further enables the precise determination of metal-dielectric barrier height and additional material parameters. The atomistic calculations also provide detailed information about the trapping mechanisms that are not accessible experimentally and could prove useful in defect engineering. For this specific illustrative example, the model has been used to interpret charging transients in a-Si_3N_4, but the framework based on first-principles simulations, continuum model, and experimental measurements are applicable to all amorphous dielectrics and other materials in general. Such multiscale, physics-based models are expected to play an increasingly central role in assessing performance and reliability of devices.

ACKNOWLEDGMENTS

The authors acknowledge Andrew Kovacs and Dimitrios Peroulis for fabrication of the a-Si_3N_4-based MIM capacitors used for measurements in this paper. This work was partly supported by Purdue's PRISM Center funded by the US Department of Energy's National Nuclear Security Administration under contract Award No. DE-FC52-08NA28617 and by the Microelectronics Advanced Research Corporation and its Focus Center on Materials, Structures, and Devices. Computational resources of nanoHUB.org are gratefully acknowledged.

APPENDIX A: ADDITIONAL TRAPPING MECHANISMS

Apart from those described in Sec. II A, there are few other charge trapping mechanisms related to relaxations labeled as "O" (other relaxations) and shallow defects indicated in Figs. 1(a) and 1(b). In addition to relaxation described in Fig. 2(a), a III-Si defect, on trapping an electron, can form an additional bond with an adjacent ideal bonded N to form a new over-coordinated N defect. In this process, the hybridization of both Si and N change from an sp^2-planar configuration to an sp^3-tetrahedral configuration. This relaxation leads to a deep-level trap with ionization energy around 4.6 eV (1.5 eV from CB edge), as shown in Fig. 1(b). Figure 5(b) shows the atomic relaxation involved when IV-Si in an edge-sharing tetrahedron traps an electron to form III-Si and V-Si defect pair. On trapping a charge, the IV-Si relaxes its strain by breaking away from the edge-sharing tetrahedron to form an

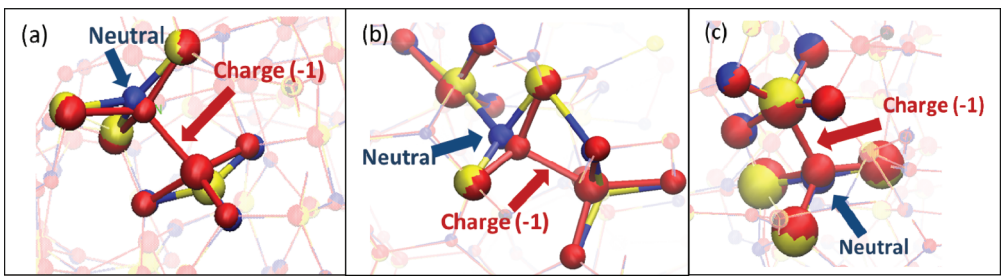

FIG. 5. (Color online) (a) A III-Si defect traps an electron and forms an additional bond with ideal bonded N. (b) Electron trapping by ideally coordinated Si (IV-Si) in an edge-sharing tetrahedron leads to an under-coordinated Si (III-Si) and an over-coordinated Si (V-Si) defect pair. (c) Electron trapping leads to formation of additional bond and over-coordinated (V-Si and IV-N) defect pair.

under-coordinated III-Si. In this process, the neighboring N atom rearranges itself and back-bonds with a IV-Si atom to form an over-coordinated (V-Si) defect, consequently forming a III-Si–V-Si defect pair. This relaxation leads to an energy level at 0.8 eV from the CB edge. Interestingly, in an another configuration involving an edge-sharing tetrahedron, ideally coordinated Si and N atoms trap an electron to form an additional bond leading to an over-coordinated (V-Si and IV-N) defect pair [see Fig. 5(c)]. This leads to a shallow trap level at 0.3–0.6 eV below the CB edge (i.e., thermodynamic ionization energies between 3.3–3.6 eV), shown in Fig. 1(b).

APPENDIX B: EXPRESSIONS FOR CURRENT FLUXES

In this section, we summarize the expressions for calculating the current fluxes for injection, leakage, and emission [J_{in}, J_{out}, and J_e (Eqs. (1)–(3))] and the corresponding flux coefficients Γ_{in}, Γ_{out}, and Γ_e, respectively.

The injection flux coefficient $\Gamma_{\text{in}}(x,E)$ is given by

$$\Gamma_{\text{in}}(x,E) = \int_{-\infty}^{\infty} \frac{4\pi m^*\sigma}{h^3}\tilde{T}(x,\mathbf{E})\beta_1(x,E,\mathbf{E})S(\mathbf{E})f(\mathbf{E})d\mathbf{E}, \tag{A1}$$

$$\tilde{T}(x,\mathbf{E}) = \exp\left(-\frac{2}{\hbar}\int_0^x \sqrt{2m^*(\Phi_B - q\phi(x') - E)}dx'\right), \tag{A2}$$

where $\tilde{T}(x,\mathbf{E})$ is the WKB tunneling coefficient for an electron tunneling through the dielectric barrier for distance x at energy $\mathbf{E}$, m^* is the effective mass for tunneling of an electron in the dielectric, σ is the tunneling capture cross-section, $\beta_1(x,E,\mathbf{E})$ is the inelastic scattering coefficient for electron injection from the contact at energy $\mathbf{E}$ to the traps located at energy E, and $S(\mathbf{E})$ and $f(\mathbf{E})$ are the supply function and Fermi-Dirac statistical distribution at contact for electron injection from the contact at energy $\mathbf{E}$. Note that $\tilde{T}$ depends on the barrier height, m^*, and the applied voltage V; β_1 depends on the trapdepth(s), ϕ_b, V, and the ambient temperature T; S and f depends on T.

Similarly, the leakage flux coefficient $\Gamma_{\text{out}}(x,E)$ can be expressed as follows:

$$\Gamma_{\text{out}}(x,E) = \int_{-\infty}^{\infty} \frac{4\pi m^*\sigma}{h^3}\tilde{T}(x,\mathbf{E})\beta_2(x,E,\mathbf{E})S(\mathbf{E}) \times [1 - f(\mathbf{E})]d\mathbf{E}, \tag{A3}$$

where $\beta_2(x,E,\mathbf{E})$ is the inelastic scattering coefficient for electron leakage from the traps at energy E to the contact at energy $\mathbf{E}$, and other terms have the same meaning as described above.

The flux-coefficient for emission Γ_e for a trap located at energy E is derived using the FP emission rate,

$$\Gamma_e(x,E) = \gamma \exp\left(-\frac{E}{k_BT} + \frac{q}{k_BT}\sqrt{\frac{qE(x)}{\pi\epsilon_0\epsilon}}\right), \tag{A4}$$

where γ is the attempt to escape frequency, $E(x)$ is the electric field at position x, and ϵ is the dielectric constant seen by the escaping electron. As explained in Ref. 11, all the flux coefficients can be approximated to obtain closed-form analytical expressions, which reduce the computational burden significantly.

TABLE II. Ranges for parameters being optimized by simulated annealing.

Variable	Range
Barrier height Φ_B (eV)	1.2–2.2
Trap density N_T (m^{-3})	1×10^{22}–1×10^{25}
Effective mass m^*	0.1–0.6
Capture cross section σ (m^2)	1×10^{-22}–1×10^{-19}
Escape attempt frequency γ (s^{-1})	1×10^{11}–1×10^{14}
Dielectric constant ϵ	3–7
Activation energy E_a (eV)	0.0–1.0
Trap depth Φ_T (eV)	0.7–2.2

APPENDIX C: SIMULATED ANNEALING OPTIMIZATION

The cost function for determining goodness of fit used in the simulated annealing optimization procedure is given by

$$C = \sqrt{\frac{1}{N}\sum_{i=1}^{N}\left(\frac{J_i^S - J_i^E}{s_i}\right)^2},$$

where J_i^S and J_i^E are the simulated and the experimentally measured transients for data point i, s_i indicates standard deviation for the four consecutive measurements at data point i, and N is the number of experimental data points.

We have measured transients at four different temperatures (300 K, 320 K, 340 K, and 360 K) at three different voltages (10 V, 15 V, and 20 V) and at approximately 200 time points between 1 s and 100 s. We interpolate our experimental data to 20 equally spaced time intervals between 3 s and 99 s for simulated annealing optimization. We therefore have $N = 20\times4\times3 = 240$ independent data points that are used for optimization. Each transient has been measured four consecutive times to check for repeatability. The standard deviation for the four consecutive measurements at data point i is given by s_i.

We summarize the range of values for parameters being optimized using simulated annealing in Table II and justify them below.

(1) Barrier height (Φ_B): The electron injecting contact used in the MIM capacitor is a Au/Ti alloy, the composition of which is not known. The difference in work-function between Au and Ti is approximately 1 eV.[36] This justifies the range of the values of Φ_B thus used. The values of Φ_B have been estimated from the reported band structure of **a**-Si_3N_4 (Ref. 34).

(2) Trap density (N_T): Reported trap densities in **a**-Si_3N_4 lie in the range of 10^{22}–10^{26}m^{-3} (Ref. 37 and 38).

(3) Effective mass (m^*): Reported effective masses in **a**-Si_3N_4 lie in the range of 0.2–0.5 eV (Refs. 39 and 40).

(4) Capture cross section (σ): The capture cross section used here is the effective area offered by a trap for a tunneling electron. These values are typically lower than electron capture from the CB. The reported capture cross section values for trap-assisted tunneling in insulators lie on the order of $10^{-20}\,\text{m}^2$ (Ref. 41).

(5) Attempt to escape frequency (γ): The attempt to escape frequency is capped by the phonon vibration frequency [$\sim 10^{14}\ \text{s}^{-1}$ (Ref. 42)]. However, the values typically used are lower and lie between $10^{11}\ \text{s}^{-1}$ and $10^{14}\ \text{s}^{-1}$.

(6) Dielectric constant (ϵ): This is the effective dielectric constant seen by a captured electron trying to escape to the CB. The range varies between the low frequency electrical dielectric constant to the high frequency optical dielectric constant[43] values.

(7) Activation energy (E_a): The range of reported values for activation energy for defect generation in **a**-Si_3N_4 varies between values of 0.2 and 0.42 (Refs. 44 and 45).

(8) Trap depth (Φ_T): The range of trap depths used for simulated annealing optimization using a single trap level [Fig. 3(a)] is the same range of most effective defect levels obtained from first-principles calculations [Fig. 1(c)]. These levels are also consistent with TSCIS experiments.[24]

APPENDIX D: SENSITIVITY ANALYSIS

Sensitivity is defined as follows:

$$S_P(t) = \frac{1}{J(t)} \frac{\delta J(t)}{\delta P} \Delta P,$$

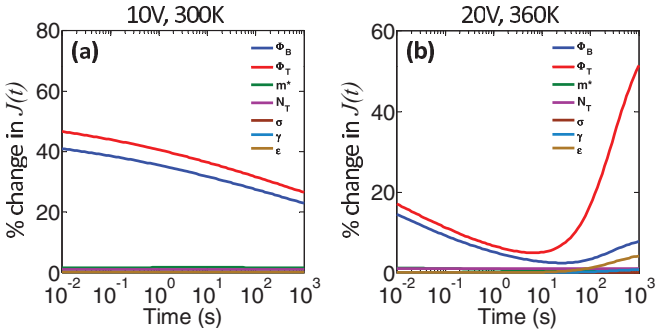

FIG. 6. (Color online) Sensitivity of the transient leakage current to a 1% change in each of the input parameters for the two extremes of voltage biases and temperatures used in the experimental data; (a) 10 V, 300 K and (b) 20 V, 360 K. Φ_T is determined to be the most sensitive input parameter, followed by Φ_B.

where $S_P(t)$ is the sensitivity of parameter P on leakage current J at time t, and ΔP is the uncertainty in the value of P, assumed to be 1% for the sensitivity analysis summarized in Fig. 6.

*alam@purdue.edu
†Corresponding author: strachan@purdue.edu

[1]G. M. Rebeiz and J. B. Muldavin, IEEE Microw. Mag. **2**, 59 (2001).
[2]I. Fujiwara, H. Aozasa, A. Nakamura, Y. Komatsu, and Y. Hayashi, Tech. Dig. Int. Electron Devices Meet., 995 (1998).
[3]J. Schmidt, M. Kerr, and A. Cuevas, Semicond. Sci. Technol. **16**, 164 (2001).
[4]J. Palm, V. Probst, A. Brummer, W. Stetter, R. Tolle, T. P. Niesen, S. Visbeck, O. Hernandez, M. Wendl, H. Vogt, H. Calwer, B. Freienstein, and F. Karg, Thin Solid Films **431–432**, 514 (2003).
[5]D. L. Smith, *Thin-Film Deposition: Principles and Practice* (McGraw-Hill, New York, 1995).
[6]M. J. Powell, C. van Berkel, A. R. Franklin, S. C. Deane, and W. I. Milne, Phys. Rev. B **45**, 4160 (1992).
[7]U. Zaghloul, G. Papaioannou, F. Coccetti, P. Pons, and R. Plana, Microelectron. Reliab. **49**, 1309 (2009).
[8]C. Groves, J. C. Blakesley, and N. C. Greenham, Nano. Lett. **10**, 1063 (2010).
[9]J. Cai and C.-T. Sah, IEEE Trans. Electron Devices **20**, 60 (1999).
[10]R. E. Paulsen and M. H. White, IEEE Trans. Electron Devices **41**, 1213 (1994).
[11]S. Palit and M. A. Alam, J. Appl. Phys. **111**, 054112 (2012).
[12]P. E. Blöchl and J. H. Stathis, Phys. Rev. Lett. **83**, 372 (1999).
[13]N. L. Anderson, R. P. Vedula, P. A. Schultz, R. M. Van Ginhoven, and A. Strachan, Phys. Rev. Lett. **106**, 206402 (2011).
[14]R. P. Vedula, N. L. Anderson, and A. Strachan, Phys. Rev. B **85**, 205209 (2012).
[15]P. A. Schultz, Phys. Rev. Lett. **84**, 1942 (2000).
[16]P. A. Schultz, Phys. Rev. Lett. **96**, 246401 (2006).
[17]W. Jost, J. Chem. Phys. **1**, 466 (1933).
[18]P. A. Schultz and O. A. von Lilienfeld, Model. Simul. Mater. Sci. Eng. **17**, 084007 (2009).
[19]N. L. Anderson, R. P. Vedula, P. A. Schultz, R. M. V. Ginhoven, and A. Strachan, Appl. Phys. Lett. **100**, 172908 (2012).
[20]J. P. Perdew, K. Burke, and M. Ernzerhof, Phys. Rev. Lett. **77**, 3865 (1996).
[21]http://dft.sandia.gov/quest/, R. P. K. Vedula, G. Bechtol, B. P. Haley, and A. Strachan, Nanomaterials Seqquest DFT (http://nanohub.org/resources/3982) (2010).
[22]N. Troullier and J. L. Martins, Phys. Rev. B **43**, 1993 (1991).
[23]D. R. Hamann (unpublished).
[24]A. Suhane, A. Arreghini, R. Degraeve, G. Van den bosch, L. Breuil, M. B. Zahid, M. Jurczak, K. De Meyer, and J. Van Houdt, IEEE Electron Device Lett. **31**, 77 (2010).
[25]V. A. Gritsenko, S. S. Nekrashevich, V. V. Vasilev, and A. V. Shaposhnikov, Microelectron. Eng. **86**, 1866 (2009).
[26]J. Robertson, Philos. Mag. B **69**, 307 (1994).
[27]G. Pacchioni and D. Erbetta, Phys. Rev. B **60**, 12617 (1999).
[28]G. Pacchioni and D. Erbetta, Phys. Rev. B **61**, 15005 (2000).
[29]L. Giacomazzi and P. Umari, Phys. Rev. B **80**, 144201 (2009).
[30]R. Tsu and L. Esaki, Appl. Phys. Lett. **22**, 562 (1973).
[31]S. C. Miller and R. H. Good, Phys. Rev. **91**, 174 (1953).
[32]J. Frenkel, Phys. Rev. **54**, 647 (1938).
[33]T. J. Drummond, *Work Functions of the Transition Metals and Metal Silicides* (Sandia National Labs, 1999), http://www.osti.gov/scitech/servlets/purl/3597.
[34]G. D. Wilk, R. M. Wallace, and J. M. Anthony, J. Appl. Phys. **89**, 5243 (2001).
[35]See Supplemental Material at http://link.aps.org/supplemental/10.1103/PhysRevB.88.205204 for additional information and simulation results.
[36]Y. Hirose, A. Kahn, V. Aristov, P. Soukiassian, V. Bulovic, and S. R. Forrest, Phys. Rev. B **54**, 13748 (1996).
[37]T. Searle (ed.), *Properties of Amorphous Silicon and Its Alloys* (INSPEC/IEE, London, 1998).
[38]W. L. Warren, J. Kanicki, J. Robertson, E. H. Poindexter, and P. J. McWhorter, J. Appl. Phys. **74**, 4034 (1993).

[39]V. A. Gritsenko, E. E. Meerson, and Y. N. Morokov, Phys. Rev. B **57**, R2081 (1998).
[40]T. P. Ma, IEEE Trans. Electron Devices **45**, 680 (1998).
[41]I. Lundstrom and C. Svensson, J. Appl. Phys. **43**, 5045 (1972).
[42]W. C. Johnson, IEEE Trans. Nucl. Sci. **19**, 33 (1972).
[43]M. Klanjšek Gunde and M. Maček, Phys. Status Solidi A **183**, 439 (2001).
[44]E. D. Tober, J. Kanicki, and M. S. Crowder, Appl. Phys. Lett. **59**, 1723 (1991).
[45]M. Koutsoureli, E. Papandreou, L. Michalas, and G. Papaioannou, Microelectron. Eng. **90**, 145 (2012).